# Numerical Model of the Plasma Sheath Generated by the Plasma Source Instrument Aboard the Polar Satellite

**Wing C. Leung and Nagendra. Singh**
Department of Electrical and Computer Engineering
The University of Alabama in Huntsville, Alabama, 35899

**Thomas. E. Moore**
National Aeronautics and Space Administration
Goddard Space Flight Center, Greenbelt, MD 20771

**Paul D. Craven**
National Aeronautics and Space Administration
Marshall Space Flight Center, Huntsville, AL 35812

**Abstract**. The plasma sheath generated by the operation of the Plasma Source Instrument (PSI) aboard the POLAR satellite is studied by using a 3-dimensional Particle-In-Cell (PIC) code. When the satellite passes through the region of low density plasma, the satellite charges to positive potentials as high as 40-50Volts due to the photoelectrons emission. In such a case, ambient core ions cannot accurately be measured or detected. The goal of the onboard PSI is to reduce the floating potential of the satellite to a sufficiently low value so that the ions in the polar wind become detectable. When the PSI is operated, an ion-rich Xenon plasma is ejected from the satellite, such that the floating potential of the satellite is reduced and is maintained at about 2Volts. Accordingly, in our 3-dimensional PIC simulation, we considered that the potential of the satellite is 2Volts as a fixed bias. Considering the relatively high density of the Xenon plasma in the sheath ($\sim 10-10^3 \mathrm{cm}^{-3}$), the ambient plasma of low density ($< 1 cm^{-3}$) is neglected. In the simulations, the electric fields and plasma dynamics are calculated self-consistently. We found that an "Apple" shape positive potential sheath forms surrounding the satellite. In the region near the PSI emission, a high positive potential hill develops. Near the Thermal Ion Detection Experiment (TIDE) detector away from the PSI, the potentials are sufficiently low for the ambient polar wind ions to reach it. In the simulations, it takes about a hundred electron gyroperiods for the sheath to reach a quasi-steady state. This time is approximately the time taken by the heavy $Xe^+$ ions to expand up to about one average Larmor radius of electrons from the satellite surface. Using the steady state sheath, we performed trajectory calculations to characterize the detector

response to a highly supersonic polar wind flow. The detected ions' velocity distribution shows significant deviations from a shifted Maxwellian in the ambient polar wind population. The deviations are caused by the effects of electric fields on the ions' motion as they traverse the sheath.

## 1. Introduction

The launch of the Global Geospace Science POLAR satellite is a part of the International Solar Terrestrial Physics (ISTP) project, which is concerned with the measurement of the low density plasma, low and high energy particles and fields in the high latitude polar regions of the magnetosphere. When the POLAR satellite orbit covers the high altitude polar cap region, it becomes positively charged owing to the low density of the plasma and the emission of electrons by the photoelectric effects of sunlight shining on the satellite surface. In this situation, the floating potential of the satellite reaches up to 40 to 50 Volts, such that low energy or ambient core plasma can not accurately be measured or detected. Therefore, instrumentation consisting of the Thermal Ion Detection Experiment (TIDE) and Plasma Source Instrument (PSI) was developed to meet the requirement of the ISTP program regarding the measurement of the low energy ambient plasma in the magnetosphere. When the onboard PSI is operated, a low energy ion-rich plasma, which consists of Xenon ions and electrons along with the neutral Xenon gas, is emitted from the bottom (-z) of the satellite. This plasma provides the ion current to balance the photoelectron current, lowering the satellite potential to about 2Volts as established by the measurements. With such a relatively low floating potential on the satellite surface, the TIDE is able to detect a substantially large amount of ion flux even in the regions of very low plasma densities in the magnetosphere. Since the plasma sheath generated by the operation of the PSI and the effects of electric fields in the sheath on the ions' motion are unknown, the velocity distribution of the detected ions with PSI on is uncertain.

The purpose of this paper is to study the plasma sheath generated by the operation of the PSI on the POLAR satellite by means of a fully 3-dimensional Particle-In-Cell (PIC) code. In the simulation, the satellite surface potential is fixed at 2Volts as indicated by the measurements when PSI is on. Since the ambient plasma density ($\approx 0.1 cm^{-3}$) is several orders of magnitude smaller than the density of the PSI generated plasma in the

sheath, the effect of the ambient plasma in the sheath is ignorable and it is not included; only the photoelectrons and the PSI generated ion-rich plasma are considered in the simulations. The electric fields and plasma dynamics are calculated self-consistently. In this paper we discuss the distributions of the plasma and the electric fields in the sheath structure. The electric fields in the sheath are shown to produce electrons having energies up to a few tens of eV due to the $\underline{E}\times\underline{B}$ drift. Furthermore, the expansion of the plasma is seen to produce $Xe^+$ with energies up to ~100eV.

We also performed particle trajectory calculations to characterize the TIDE detector response to a highly supersonic polar wind flow by using the steady state sheath with the PSI on. The modifications in the ions' velocity distribution due to the sheath are analyzed, suggesting that significant distortions in the ion velocity distribution function produced by the electric fields in the sheath must be considered when analyzing data from TIDE.

## 2. Simulation Technique

We performed three-dimensional simulations of photoelectrons and ion-rich plasma ejected from a satellite as schematically shown in Figure 1. The satellite is a conducting cylinder of height h and diameter d, and is located at the center of the simulation box. The simulation box is a cylinder of height $2z_{max}$ and radius $r_{max}$. The magnetic field ($\underline{B}$) is along the x axis. In this geometry, the satellite spins around the z axis. Photoelectrons are ejected from the top and the entire half-cylindrical surface given by $r = d/2$ and $-\pi/2 \le \theta \le \pi/2$, where $\theta$ is measured from the x direction; dotted arrows indicate the ejection of the photoelectrons. We denote the photoelectron temperature and current by $T_{ph}$ and $I_{ph,}$ respectively. Besides the photoelectrons in the simulation, we also consider the PSI generated ion-rich plasma. This plasma consists of Xenon ions ($X_e^+$) and electrons, and is ejected from the bottom of the satellite. The downward arrow indicates the PSI ejection in the negative z direction. The PSI location is more clearly shown in the expanded scale of the bottom of the satellite (see Fig. 1). The electron and ion temperatures of the Xenon plasma are denoted by $T_e$ and $T_{i,}$ respectively. The electron and ion currents generated by the PSI are $I_e$ and $I_{Xe}$, respectively. The simulation was performed by using macroparticles each having a charge and mass

equivalent to a large number, say $\eta$ (~$10^7$), of real plasma particles. The real Xenon ion to electron mass ratio $m_i / m_e$ was used in the simulation. In order to establish the photoelectron and PSI emitted currents, we ejected a certain number of electrons and ions in the form of macroparticles at each time step.

The potential distribution $\Phi(r,\theta,z)$ was determined by solving Poisson equation. First we performed a Fourier transform of $\Phi(r,\theta,z)$ with respect to the azimuthal angle $\theta$. This reduced the three-dimensional Poisson equation to a two-dimensional one in r and z for each Fourier component. Each such two-dimensional Poisson equation was approximated by a set of five point difference equations. The sparse matrix of the resulting system of linear equations were solved by the conjugate gradient method [Hestenes and Stiefel, 1952]. The solution of the linear equation was Fourier-inverted to obtain $\Phi(r,\theta,z)$. The boundary conditions on $\Phi(r,\theta,z)$ are as follows. The satellite surface potential is fixed at a known potential $\Phi_o$ while the outer boundaries of the simulation box are at zero potential, i.e., $\Phi(r = r_{\max},\theta,z) = \Phi(r,\theta,|z| = z_{\max}) = 0$. In order to maintain the center body potential $\Phi_o$, the photoelectron current and PSI current have to balance each other, i.e., $I_{Xe} = I_{ph} + I_e$. We point out here that ideally the problem should be solved with $\Phi_o$ as a floating potential self-consistently determined by currents ejected and returned to the body. However, in such a case the floating boundary conditions changes the nature of the sparse matrix and its inversion becomes a difficult task. We are currently working on the inversion of such a matrix.

The evolution of the plasma was calculated by solving the equation of motion of the computer electrons and ions in the self-consistent electric fields and the ambient magnetic field. The charged particles' motions were advanced in each time step $\Delta t$ using the leapfrog technique [Morse, 1970]. The macroparticles leaving the simulation box or impacting the satellite were discarded. Near the PSI aperture, the neutral gas density is very high, and electrons are collisional; the electron-neutral collisions are found to play a significant role in the dynamics of electrons in the near zone of the PSI emission. The collisions effectively slow down the PSI-emitted electrons and therefore they are found to be essential in developing a numerically stable algorithm for the electron motion with reasonable time steps.

We also performed trajectory calculations to characterize the modifications in the velocity distribution function of the ions in ambient polar wind type of flow when the ions are eventually collected by the TIDE. We used the steady state sheath with and without the PSI operation. In this trajectory simulation, hydrogen ions $H^+$ are injected in the outer boundaries of the cylindrical surface given by $r = r_{max}$, $-5^o \le \theta \le 5^o$ and $|z| \le 20m$ (see figure 1). These ions represent polar wind ions of temperature $T_o$ with a beam velocity $U_o$ along the negative x direction. Only the ions impacting the top surface of the satellite are considered as detected, and their velocities in the initial polar wind and at the time of the impact on the surface are recorded for the purpose of constructing distribution functions.

## 3. Numerical Results

The simulation was performed for the following parameters: $\Phi_o$=2Volts, photoelectron temperature $T_{ph}$=1eV, PSI-emitted electron temperature $T_e$=1eV, $Xe^+$ ion beam temperature $T_i$=0.5eV and beam velocity = 5.4km/s for 20eV beam energy, satellite body height h=1.8m and diameter d=2.4m, the ambient magnetic field $\underline{B}$=100nT, photoelectron current $I_{ph}$=30μA, PSI-emitted electron current $I_e$=70μA, and ion current $I_{Xe}$=100μA (typical values for PSI in the keeper only mode, the usual operating mode), and time step Δt=1.1μs. The simulation was performed for a Xe plasma with ion to electron mass ratio $M/m_e$ = 240516. The simulation box dimensions are $r_{max}$=240m, and $z_{max}$=234m. The axial and radial grid sizes ranged from 0.24m near the satellite surface to about 1m near the outer boundaries of the simulation box. For the magnetic field $\underline{B}$ =100nT, the electron cyclotron period $\tau_{ce} \cup 0.36ms$, and electron Larmor radius $\rho_e \cup 34m$ for 1eV electrons.

The macroparticles are injected from the satellite surface carrying the respective currents $I_{ph}$, $I_e$, and $I_{Xe}$. The number of injected particles is related to the real electrons and ions in the following way: if one macroion carries a charge *q*, then it is equivalent to η real ions given by $\eta = q/e$. The ion current injected is $I_i = q\Delta N_i / \Delta t$, where $\Delta N_i$ is the number of macro ions ejected during a time step Δt. Thus $\eta = I_i \Delta t / e(\Delta N_i)$. Δt is determined by the stability criteria of the numerical algorithms; typically we have

$\Delta t \cong 0.1\Omega_e^{-1}$, $\Omega_e$ being the electron cyclotron frequency. $\Delta N_i$ is determined by the overall capability of the computers in handing the number of particles and also by the CPU considerations. In the runs described here $\Delta N_i = 72$ and $\eta=10^7$. Correspondingly, $\Delta N_{ph} = 22$ and $\Delta N_e = 50$ for the photo and PSI-emitted electrons.

The simulation begins at $t = 0$ with no plasma in the simulation box. When $t > 0$, photoelectrons and PSI generated ion-rich plasma were ejected from the surface of the satellite as mentioned earlier. In the simulation, it took about a hundred electron gyroperiods for the sheath to reach a quasi-steady state. After reaching the quasi-steady state the sheath continues to evolve, although extremely slowly and only in the outer regions of the sheath. The core of the sheath remains almost unchanged after this initial stage lasting about $100\tau_{ce} \cup 36ms$. This quasi-steady state sheath structure is described in the following section.

3.1 Electron Distribution in the Sheath

Figures 2a, 2b and 2c show the spatial distribution of electrons in three principal planes x-z, y-z, and x-y, respectively. Note that there is an electron cloud consisting of a dense core near the satellite and a halo covering a relatively large volume around it. There are some noteworthy features of both the core and the halo. First of all we note that the size of the core in all the principal planes is ~65m, which is about twice the gyroradius of the electrons ($\rho_e \cup 34m$) emitted from the satellite with a thermal energy of 1eV. The gyroperiod of the electrons in 100nT magnetic field is 0.36ms. Therefore, the electrons quickly spread out to distance of about $\rho_e$ in the y-z plane. The ions follow the electrons rather slowly because of their heavy mass. Since at the time scale of the evolution of the sheath the ions are nearly unmagnetized, they expand nearly isotropically, barring their directed motion in the negative z direction near the PSI emission. However, such ions are quickly retarded by the large developing potentials supported by the positive space charge created by the ions themselves. The expansion time for the ions up to a distance $\Delta r \sim \rho_e$ is given by $\Delta t \cong \rho_e / V_{ti}$, where $V_{ti}$ is the ion thermal velocity which for 0.5eV $Xe^+$ ions is about 0.86km/s. This estimate for $\Delta t$ is

about 40ms, which is in good agreement with the time for the sheath to reach the quasi-steady state as mentioned above.

As expected, the halo extends to large distances along the magnetic field lines passing through the satellite (see Figures 2a and 2c). The electrons reaching to large value of |x| are the relatively fast electrons which are not confined by the electric fields in the sheath. Figures 2b and 2c show that the halo has an asymmetry about y=0; there are more electrons for y>0 than for y<0. We find that the primary cause of this asymmetry is the $\underline{E}\times\underline{B}$ drift of the electrons in the self-consistent potential structure in the sheath. As we shall show later, near the satellite surface a strong $E_z$ component of the electric field develops and it causes the photoelectrons to drift in the +y direction. This asymmetry leads to an asymmetry in the potential distribution around the satellite as discussed later.

3.2 Ion Distribution in the Sheath.

The quasi-steady distributions of ions in the sheath are shown in Figures 3a, 3b, and 3c for x-z, y-z, and x-y principal planes, respectively. Contrasting Figures 2a, 2b, and 2c with Figures 3a, 3b, and 3c, we note that the ions occupy a much smaller volume around the satellite compared to the electrons, the major difference being the absence of the halo for distances $r > \rho_e$. As noted earlier, Figures 3a and 3c show that the shape of the ion cloud is primarily determined by the electron Larmor radius; when ions ejected from PSI expand out to $r \sim \rho_e$, the sheath achieves a quasi-steady state. We have further confirmed this by performing a simulation by increasing $\underline{B}$ from 100nT to 200nT. In the latter case, the size of the ion cloud is nearly halved. We note from Figures 3a, 3b, and 3c that the ion cloud has its own core and halo; the ion core occurs just near the bottom of the satellite where PSI ejects the ion-rich plasma. The halo for the ions roughly corresponds to the core of the electrons.

The shape of the ion clouds in all the principal planes show some special features. We note the asymmetry along the z axis (Figures 3a, and 3b). The ion cloud extends to relatively larger distances in the negative z direction than that in the positive z direction. This is simply a consequence of the ejection of the ion beam from the PSI in the negative z direction with a beam velocity of 5.4km/s. The self-consistent electric fields shape the motion of the ions producing the “apple” shaped structures in the x-z and y-z planes. The

difference in the shapes in the x-z and y-z plane indicates that the flow of ions in the x-y plane is not isotropic. This is clearly seen from Figure 3c; the ion cloud extends to larger distances along y than that in x and only a few ions flow all the way to the top of the satellite (x=0, y=0, z > 0.9m).

3.3 Potential and Electric Fields in the Sheath.

Figures 4a, 4b, and 4c show the potential structures in the three principal planes x-z, y-z, and x-y, respectively. Like the spatial distribution of electrons, the potential structures also show a core and a halo; in the core the potentials are positive while in the halo the potentials are negative and generally weak ($e\Phi / kT_e < 1$). If an ambient plasma is included in the simulation, it is quite possible that the weak negative potentials are neutralized. We discuss here the structures in the core of the sheath with positive potentials. Figures 5a, 5b, and 5c show the core structure on the expanded scale. These figures show that the shape of the core is nearly the same as the spatial distribution of ions shown in Figures 3a, 3b, and 3c; both in x-z and y-z planes the potential structure are apple shaped with the top of the apple being near the satellite and it extends in the negative z direction along which the ion-rich Xenon plasma is ejected from the PSI located at the bottom of the satellite. The largest potentials develop near the bottom of the satellite. A more detailed distribution of the structure in the core near the bottom of the satellite is shown in Figures 6a, 6b, and 6c which show the equipotential contours in the x-z plane at y=0, y-z plane at x=0 and x-y plane at z=-1m respectively. These figures show that a potential peak develops very close to the bottom where the PSI deposits its plasma forming a virtual anode. Figures 6a and 6c show that the peak potential is about 45Volts, which is roughly twice the ion beam energy. This peak potential diverts the flow of PSI generated plasma. The electric fields developing here lift the ions upward along the positive z axis along with the flow in x-y plane; the fields and the ion flow, which evolve during the sheath formation, self-consistently adjust to each other establishing the quasi-steady state sheath structures shown in Figures 2a to 2c, 3a to 3c, and 4a to 4c.

The TIDE lies near the top (z≈0.9m) of the satellite; Figures 5a and 5b show that the potentials near the top are generally small compared to that near the bottom. Thus ions with energies of a few eV and greater can easily reach the TIDE. Figure 7 shows the

potential distributions near the top surface of the satellite (z=0.9m) in the x-y plane. This figure in conjunction with Figures 5c and 6c show that there is a potential ridge around the satellite in the x-y plane and the ridge amplitude decreases from the bottom to the top of the satellite. Also the ridge is more pronounced for $x<0$ compared to that for $x>0$ due to the photoelectron emission from the surface at $x>0$. Figure 7 shows a throat like structure, with the throat opening for $x>0$. Thus asymmetry associated with the throat for $x<0$ and $x>0$ might cause asymmetry in the detection of ions by the TIDE. The flux coming from the antisunward direction will be hampered by the potential ridge.

The electric field instrument (EFI) aboard the POLAR constitutes a long boom of 65m, which spins with the satellite in the x-y plane. The electric field measurement using a double probe at the tip of the boom has detected asymmetry in the y component of the electric field $E_y$. This asymmetry is also seen in our model. Figure 8 shows the equipotential surfaces in the x-y plane extending all the way to a radial distance of 65m. The asymmetry is seen only in the contours with the small potentials; at y=65m the space potential is negative while at y=-65m it is positive. The tip to tip potential difference is about 0.2Volt, giving an apparent electric field $E_y$=1.5mV/m.

### 3.4 Plasma Density Distribution

The plasma density distributions in the sheath are shown in Figures 9a, 9b, and 9c. The electron ($n_e$) and ion ($n_i$) densities are plotted along the principal axes x, y, and z. Note that the densities are given in units of number of particle per $cm^3$. We note that ion density extends to distances of about ~50m from the satellite surface. In the electron halo (Figure 2a, 2b, and 2c), the density is relatively low and the halo is not well seen from the ion density plots but is seen in the plot for $n_e(x)$. In the core of the sheath the plasma is nearly quasi-neutral with $n_e \approx n_i$. Figure 9c shows that there is a total lack of ions along the principal axis z for $z>0$ above the satellite. However, this region is populated by photoelectrons. As expected, the maximum density occurs just below the satellite surface near z=-0.9m; the maximum density is about $10^3 cm^{-3}$. Figures 9a and 9b show that the quasi-neutral plasma density in the x-y plane is not azimuthully symmetric; the densities are higher along the y axis compared to that along the x axis.

## 4. Energies of Electrons and Ions.

In order to show the energetics of the ions and electrons in the sheath, we have shown their phase space plots in x-$V_x$, y-$V_y$, and z-$V_z$ planes in Figures 10 and 11, respectively. The ion phase-space plots show that on average the faster the ion, the farther it is from the satellite. At any location the ion distribution is a beam; the minimum velocity in the beam distribution increases linearly with the distance from the satellite and the maximum velocity is approximately the ion beam velocity ejected from the PSI. However, we note that there are some ions which are faster than the ion beam velocity and they appear farthest from the satellite. The faster ions are the consequence of the plasma expansion; as the dense plasma created by the PSI expands outward, faster ions are generated [Singh and Schunk, 1982]. The expansion is seen to produce $Xe^+$ ions having velocities up to about $|V_z|$=-13km/s which amounts to an energy of about 115eV.

Figure11 shows that even in the velocity space, the electrons show a core and a halo; the core is limited to relatively low speeds $|V| < 10^3$ km/s. Such electrons come from the PSI ejection and photoemission. On the other hand, the electrons in the halo have relatively fast velocities; these electrons partly represent the populations in the tails of the Maxwellian distributions ejected from the satellite either from PSI or photoemission, and partly they gain their large velocities due to the $\underline{E}\times\underline{B}$ drift. Figure 11b clearly shows that $\underline{E}\times\underline{B}$ drift of electrons for y>0 has produced velocities up to 4000km/s and energies up to about 45eV.

## 5. Sheath Produced Modifications in the Velocity Distribution Functions of the Ambient Polar Wing Ions Detected at the Satellite Surface

In order to assess the influence of the sheath on the direction of ions by the TIDE, we performed trajectory calculations. We injected $1.2\times10^5$ $H^+$ ions at the positive x boundary of the simulation box. These $H^+$ ions represent the ambient polar wind flow and have a displaced Maxwellian distribution and temperature 0.5eV. We first describe a case in which the PSI is off and satellite is charged to +10V. The polar wind beam energy is also 10eV having an average beam velocity $V_{xo}$=-44.3km/s. Figure 12a shows the ambient polar wind velocity distribution function. Figure 12b shows the initial distribution of the subset of the injected ions which are eventually collected by the

satellite near its top surface where TIDE is mounted. Note that the slow ions having relatively small parallel velocities $V_x$ are not collected, as expected. However, Figure 12b reveals an interesting feature that the ions having relatively large perpendicular velocities are also not collected by the TIDE. This is merely the reflection of the fact that ions with large angular momentum ($mV_{\perp}r$) are not able to reach the satellite. The final distribution function of the ions after detection is shown in Figure 12c. Comparing Figure 12b with 12c, it is seen that the ions are slowed down by the electric fields in the sheath. Figure 12d compares the total kinetic energies of the collected ions in the initial polar wind (solid line) and after their collection (broken line). As expected, the ions are retarded by about 10eV.

Beside the retardation of ions, the location of the TIDE on the top of the satellite also affects the perpendicular velocity distribution functions. Figures 13a, 13b, and 13c show $F(V_x)$, $F(V_y)$, and $F(V_z)$ of the polar wind ions; the dashed curves are the initial distribution in the ambient polar wind and the solid curves are the subset of the initial distribution of the polar wind ions that reach, and are collected, by the TIDE. The dotted curves show the distributions as seen at TIDE, i. e. after experiencing potential drops. Besides the shift to a small average drift velocity in the $F(V_x)$, the collected ion distributions show severe modifications. In $F(V_y)$ ions spread out as if they have undergone heating. On the other hand in $F(V_z)$, ions have gained a net drift in the +z direction. This net drift is directly related to the location of the TIDE near the top surface; for $z>0$, above the mid-plane of the satellite, there is an upward electric fields $E_z$ which accelerates the ions generating this non-zero drift in $V_z$.

When the PSI is switched on, the satellite assumes a reduced potential of +2V and the ion distribution collected by the TIDE is modified. Consider the case when the polar wind beam energy is 10eV. Figures 14a and 14b show the initial and final distributions of the collected ions in $V_x$-$V_z$ plane. Note that the initial distribution belongs to the ambient polar wind before entering the PSI-generated sheath. Figure 14a is analogous to Figure 12b. Figure 14b shows a great deal of modification in the distribution. As expected, due to the reduced potential on the satellite, the reduction in the parallel velocity $V_x$ is relatively small compared to that shown in Figure 12c for $\Phi_o$=10V. However, we see that the entire ion population is shifted upward in positive $V_z$ and the degree of shift depends

on the parallel velocity $V_x$; smaller the $V_x$ the larger is the upward shift in $V_z$. This modification is the direct consequence of the potential distribution around the satellite. In the vicinity of the satellite, there is a relatively strong upward electric field $E_z$ associated with the apple-shaped potential distributions shown in Figure 5a and 5b; the average drift in $V_z$ is about 10km/s.

When the polar wind beam energy is increased to 20eV, the upward shift in $V_z$ is somewhat reduced. Figure 15a and 15b show the initial and final distributions of the collected ions for beam energy of 20eV. The reduction in the shift in $V_z$ is clearly seen by comparing Figure 15b with Figure 14b. This reduction in the shift along with its dependence on $V_x$ clearly suggests that shift is the consequence of the acceleration of $H^+$ ions by the $E_z$ (>0) component of the electric field in the sheath as mentioned above. When $V_x$ is relatively large, the transit time of the ions across the sheath is reduced, leading to smaller net acceleration in $V_z$.

## 6. Comparison with Observations

We have done a reality check on the simulations here by comparing them to measured velocity distribution functions where the conditions between the simulation parameters and the data are matched as closely as possible. Data from the POLAR/TIDE instrument from April 19, 1996 is used and PSI was on. Figure 16 is a spectrogram of part of this day, showing a beam of ions traveling anti-parallel to the field line direction over the north polar region. The beam energy and density varies considerably over this period. We chose a time, about 1800 UT, in which the energy of the ions (H+) is about 20 eV, a condition to which the simulation was matched and for which the conditions were steady over the time for which data were averaged (one minute time scale). Since PSI is operating, the spacecraft voltage is typically about 2 volts (Comfort et. al., 1998). Because it is the measurement of the particles at the instrument that is of interest, the TIDE data has not been adjusted to account for the spacecraft potential in the calculation of phase space densities.

A comparison of the simulation and the measured phase space densities is difficult because the simulations cannot include every effect experienced by the ions in their transport from the source to the spacecraft. In the case at hand, the spacecraft is at about

9 Re geocentric distance and the ions may be subjected to a velocity filter effect that limits the highest and lowest velocities that reach the spacecraft from distant sources. Although not shown here, such a sharp cutoff at the high and low velocities is seen in the TIDE data. This effect is not included in the simulation results. In the simulations, the initial velocity distribution of the polar wind is assumed to be Maxwellian with appropriate drifts and temperatures. Figure 17 shows normalized (to the maximum) contours of the phase space densities measured by TIDE. Only those phase space densities above the noise level, determined as a constant count rate with energy, are shown. Figure 17 should be compared with Fig. 18 which shows a cut in the x-z plane of the particle distribution that reaches the instrument in the simulations. The input velocity distribution in the simulation has parameters as in Fig. 15 (20 eV beam x direction) with the addition of a 20 km/s drift in the negative z direction. Because the simulations do not include many effects experienced by the plasma, as mentioned above (e.g. velocity filter effect and noise), the measurements and the simulation can be compared only qualitatively. The measured distribution in the Vx-Vz plane shown in Figure 17 reveal that the ions detected by the TIDE have average drifts of about -60 km/s in the x direction and about -18 km/s along the z direction. However, the distribution is not Mazwellian. It is highly distorted in comparison to a Maxwell distribution; the distortion appears dependent on the parallel velocity, Vx. The spread in Vz appears to increase with increasing |Vx|. Note the slant in the contours for $Vz<0$ for $-70 < Vx < -45$ km/s. This feature is quite similar to the feature of the distribution shown in Figures 14 and 15. This feature is also seen in the Figure 18. The most striking feature of the Vz distribution is the broadening at large values of |Vx|. This is also clearly seen from Fig. 18. These features are difficult to explain analytically, but they are the consequence of the complex electric field (potential) distribution in the immediate vicinity of the spacecraft. The comparison clearly reveals that the electric field distribution that is generated by the PSI plasma and that is near POLAR, strongly affect the distribution of the collected particles.

**7. Conclusions**

The PSI generated sheath structure is simulated by using the three-dimensional particle-in-cell method. The photoelectrons and PSI-emitted ion rich plasma are included in the simulations, neglecting the ambient plasma. The sheath reaches a quasi-steady state in about hundred electron gyroperiods, which is the time taken by the PSI emitted $Xe^+$ ions to expand out to distance of about one electron Larmor radius. A slow evolution continues afterwards as the PSI generated plasma slowly expands. The distribution of electrons, ions and the potentials around the satellite are given. It is shown that the sheath consists of a core and a halo. The core has the dimensions of the order of one electron Larmor radius. It contains a quasi-neutral plasma with $n_e \cong n_i$. The electric potential is positive in the core and its size slowly increases as the PSI generated plasma expands. Electrons populate the halo with negative potentials. The core of the sheath has apple-shaped potential distributions with large potentials just below the satellite where the PSI deposits its ion-rich plasma. The maximum plasma density in this region is about $\sim 10^3 cm^3$. On the sides of the satellite, the PSI-generated plasma density is $\sim 10 cm^{-3}$.

We have shown that the electric fields in the sheath can significantly modify the velocity distribution function of the ions collected by the TIDE. The principal modification is noted in the acceleration of ions in the positive $V_z$ direction depending on the ion velocity in the x direction. As the $V_x$ component of the ion velocity increases the shift becomes less important. The shift is dependent on the transit times of the ions in the sheath.

The simulations reveal that the sheath can be a source of relatively fast electrons up to an energy of about 45eV and also fast $Xe^+$ ions with energies ~115eV. The fast electrons are produced by the $\underline{E} \times \underline{B}$ drifts in the sheath while the fast ions are the product of plasma expansion.

**Figure Captions**

**Figure 1.** The geometry of the simulation. The cylindrical satellite of height h and diameter d is at the center of the simulation box. The magnetic field $\underline{B}$ is along the x direction. The potential on the satellite is fixed $\Phi_o$ and the potential on the outer boundary of the simulation box is zero. The lower panel shows the location of the PSI at the bottom of the satellite on the expanded scale.

**Figure 2.** Electron Distribution in the three principal planes (a) x-z, (b) y-z, and (c) x-y, respectively. Note that the dense core plasma is surrounded by a halo.

**Figure 3.** Ion Distribution in the three principal planes (a) x-z, (b) y-z, and (c) x-y, respectively. Note the apple-shaped distributions in x-y and y-z planes. Even ions show the core and the halo, but the dense core of ions is below the satellite where PSI emitted the plasma. The halo of ions is the same size of the core of electrons.

**Figure 4.** The quasi-steady potential contours in the principal planes (a) x-z, (b) y-z, and (c) x-y. Note the core with the positive potential and the halo with the negative potential. The positive potential core in the sheath corresponds to the distribution of the ions in Figure 3.

**Figure 5.** The positive potential core in the potential distribution near the satellite on the expanded scale (a) x-z, (b) y-z, and (c) x-y planes.

**Figure 6.** The potential contours on expanded scale near the PSI emission in (a) x-z plane at y=0, (b) y-z plane at x=0, and (c) x-y plane at z=-1m. Note the large potentials developing near the PSI emission.

**Figure 7.** The potential contours in the x-y plane near the top (z=0.9m) surface of the satellite. Note that the potentials are relatively small near the top comparing to the bottom shown in Figure 6c.

**Figure 8.** The potential contours in the x-y plane at z=0 up to a distance of 65m from the satellite. Note that an asymmetry is along y axis.

**Figure 9.** Plasma density distribution near the satellite along the three principal axes (a) x, (b) y, and (c) z, respectively. Note that the large densities develop below the PSI emission shown in (c).

**Figure 10.** Ion phase space plots in (a) x-$V_x$, (b) y-$V_y$, and (c) z-$V_z$. Note the product of faster $Xe^+$ ions having velocity up to 13km/s.

**Figure 11.** Electron phase space plots in (a) x-$V_x$, (b) y-$V_y$, and (c) z-$V_z$. Note the product of relatively fast electron having velocity up to 4000km/s.

**Figure 12.** (a) The initial velocity distribution of the injected ions representing the ambient polar wind in $V_x$-$V_z$ plane. The beam energy is 10eV with an average beam velocity of -44.3km/s. (b) The initial, and (c) the final velocity distributions of ions which were eventually collected by the TIDE detector. Out of $1.2\times10^5$ $H^+$ ions injected in the boundary, only 170 ions were collected in the vicinity of TIDE. (d) The initial (solid line) and final (dotted line) kinetic energies of the collected ions. After collection ions lost 10eV energy.

**Figure 13.** Ion distribution functions (a) $F(V_x)$, (b) $F(V_y)$, and (c) $F(V_z)$. Distributions of the initial injected ions are shown by dashed curves. The initial distribution of the ions eventually collected by TIDE by solid curves and after collection by dotted curves.

**Figure 14**. The velocity distribution of the collected ions in $V_x$-$V_z$ plane when PSI is on (a) initial in ambient polar wind and (b) final of the collection. The polar wind beam energy is 10eV.

**Figure 15.** Same as Figure 14 but the polar wind beam energy is 20eV with an average beam velocity of –63km/s.

**Figure 16.** A spectrogram of H+ phase space density from the POLAR/TIDE instrument. The polar wind is seen as the narrow beam along the field line near 180 degrees in spin angle in the upper panel and at energies below about 100 eV in thelower panel.

**Figure 17.** Contours of normalized H+ phase space density measured by TIDE. The contours were made from the measurements taken from 1800 UT to 1801 UT in Figure 16.

**Figure 18.** Normalized contours of the velocity distribution from the simulations. Parameters are the same as in Figure 15 but with a 20 km/s drift in the negative z direction.

**References**

Comfort, R.H., T. E. Moore, P. D. Craven, C. J. Pollock, F. S. Mozer, W. S. Williamson, Spacecraft Potential Control by the Plasma Source Instrument on the POLAR Satellite, *J. Spacecraft and Rockets, 35*, 845, 1998.

Hestenes, M.R., and E. Stiefel, Methods of conjugate gradients for solving linear systems, *J. Res*. of the national bureau of standards, 49, 409, 1952.

Morse, R.L., Multidimensional plasma simulations by particle-in-cell methods, in *Computational Physics*, edited by B. Alder, S. Fernbach and M. Rotenberg, pp. 213-239, Academic, San Diego, Calif., 1970.

Singh, N., and R.W. Schunk, Numerical calculations relevant to the initial expansion of the polar wind, *J. Geophys. Res*. 87, 9154, 1982.

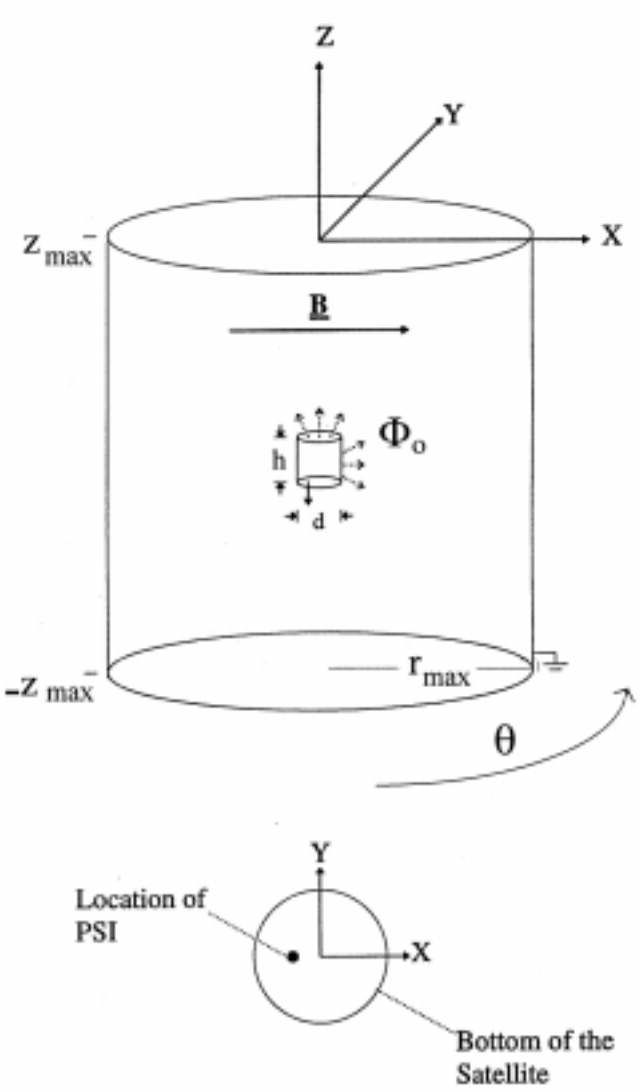


**Figure 1.** The geometry of the simulation. The cylindrical satellite of height h and diameter d is at the center of the simulation box. The magnetic field $\underline{B}$ is along the x direction. The potential on the satellite is fixed $\Phi_o$ and the potential on the outer boundary of the simulation box is zero. The lower panel shows the location of the PSI at the bottom of the satellite on the expanded scale.

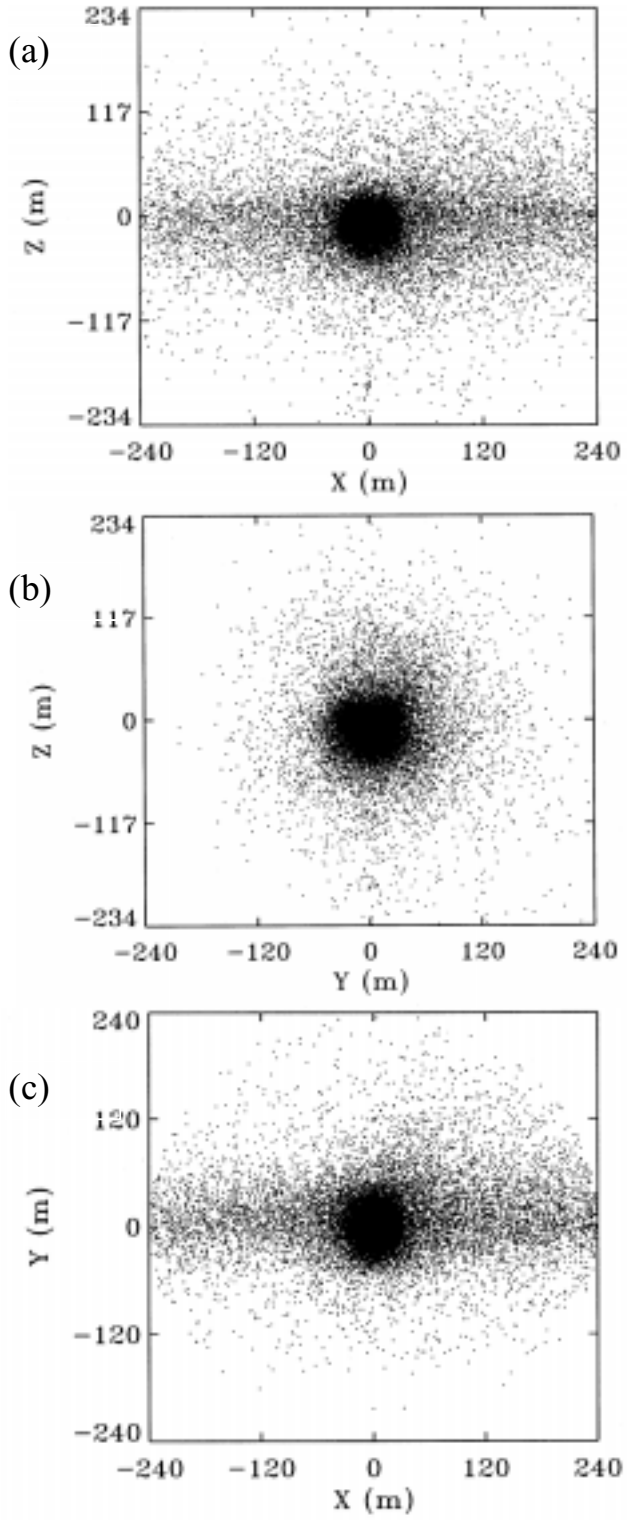


**Figure 2.** Electron Distribution in the three principal planes (a) x-z, (b) y-z, and (c) x-y, respectively. Note that the dense core plasma is surrounded by a halo.

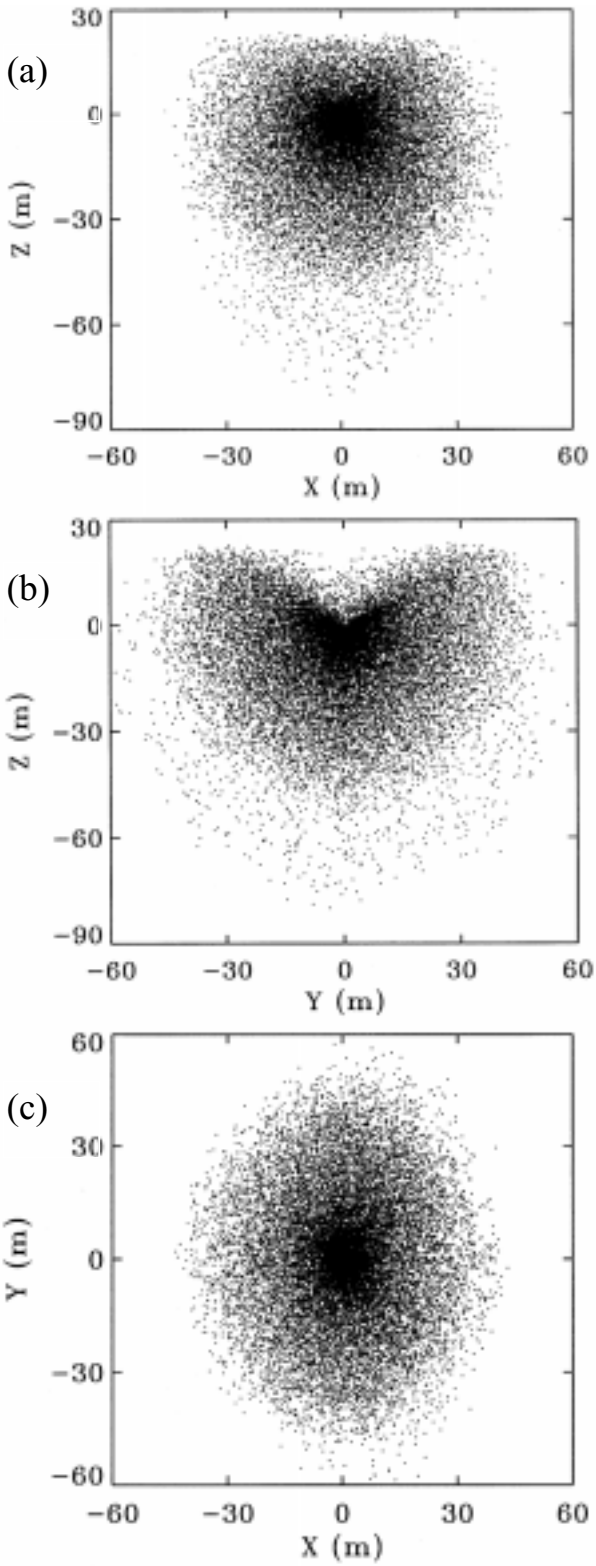


**Figure 3.** Ion Distribution in the three principal planes (a) x-z, (b) y-z, and (c) x-y, respectively. Note the apple-shaped distributions in x-y and y-z planes. Even ions show the core and the halo, but the dense core of ions is below the satellite where PSI emitted the plasma. The halo of ions is the same size of the core of electrons.

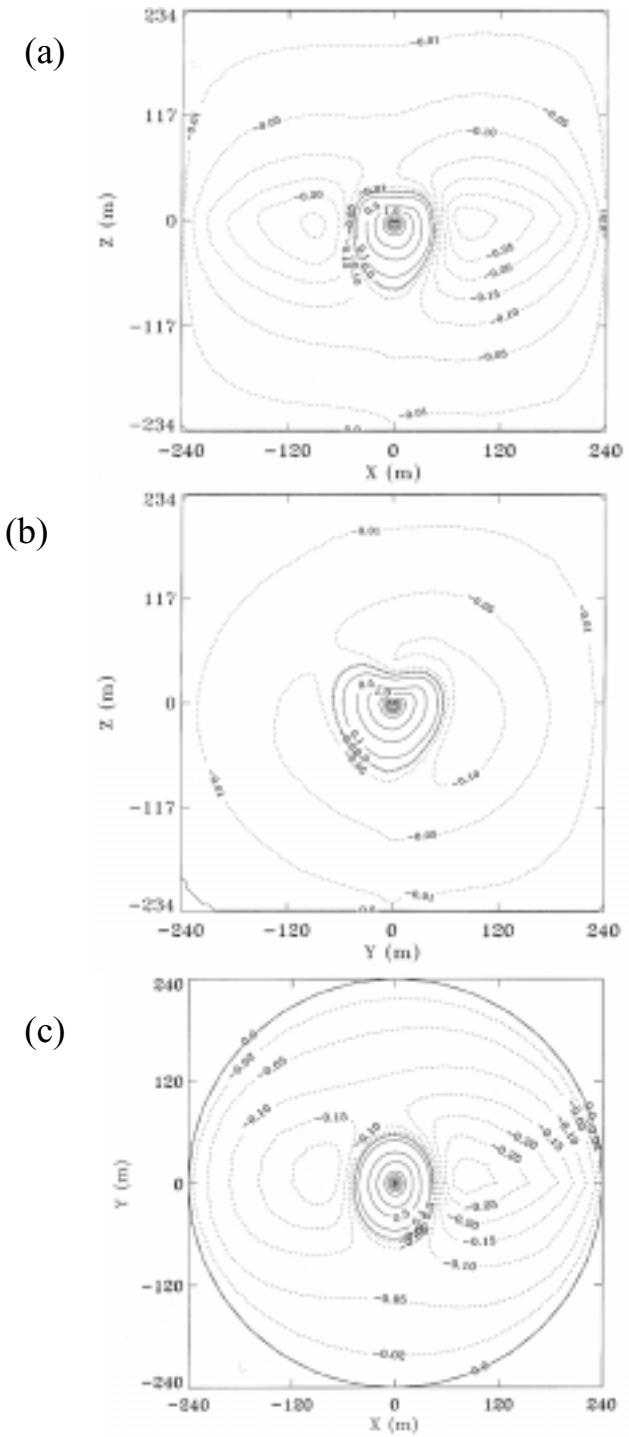


**Figure 4.** The quasi-steady potential contours in the principal planes (a) x-z, (b) y-z, and (c) x-y. Note the core with the positive potential and the halo with the negative potential. The positive potential core in the sheath corresponds to the distribution of the ions in Figure 3.

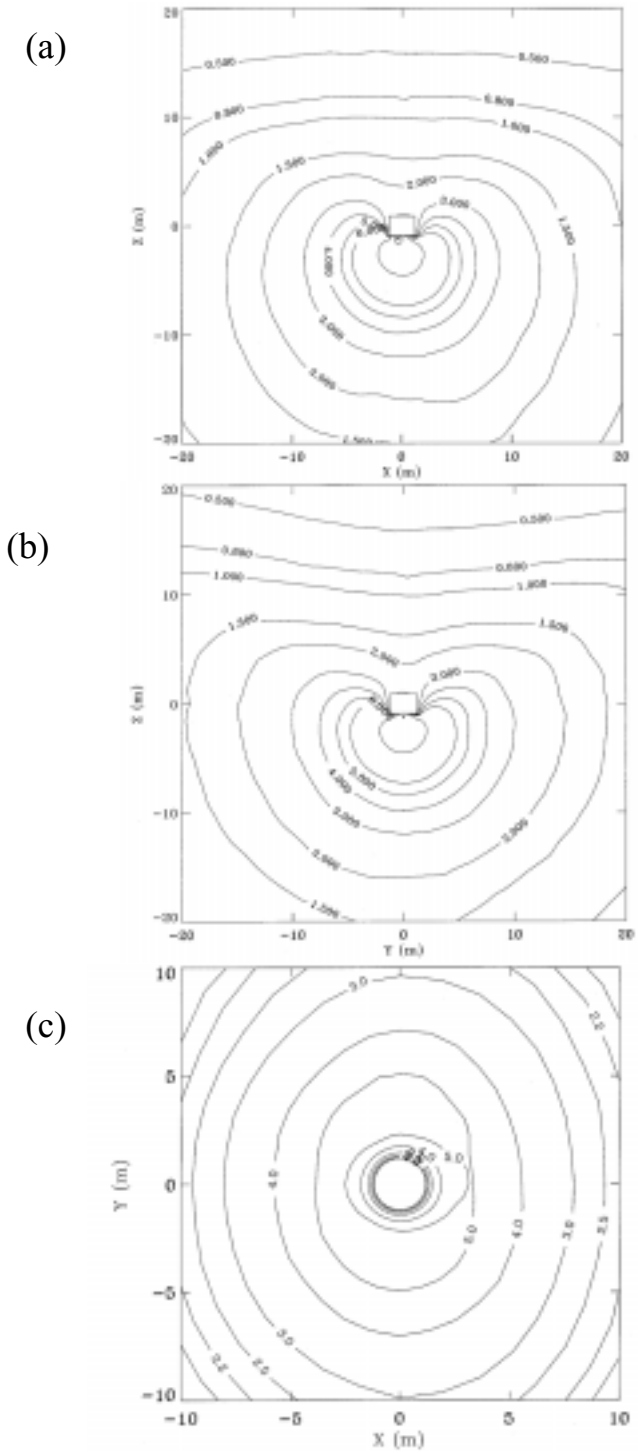


**Figure 5.** The positive potential core in the potential distribution near the satellite on the expanded scale (a) x-z, (b) y-z, and (c) x-y planes.

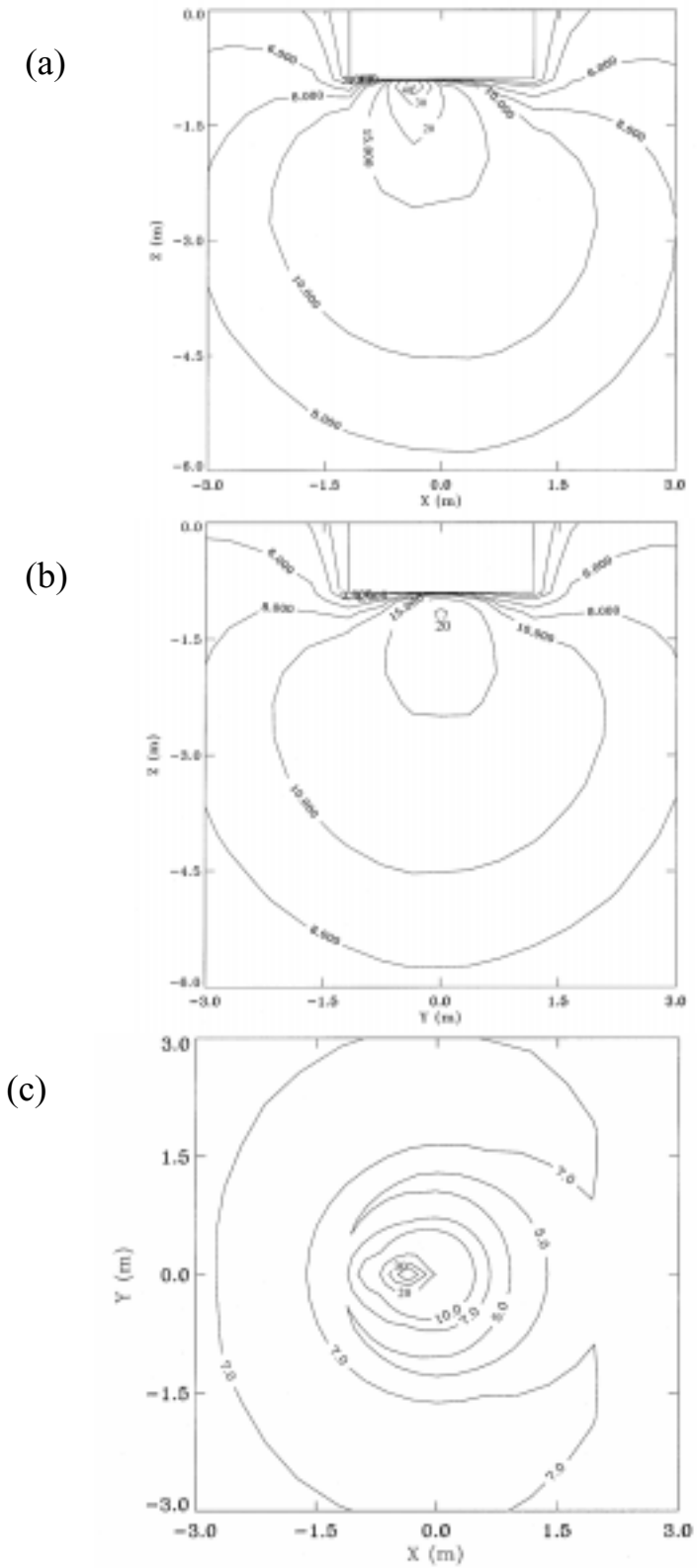


**Figure 6.** The potential contours on expanded scale near the PSI emission in (a) x-z plane at y=0, (b) y-z plane at x=0, and (c) x-y plane at z=-1m. Note the large potentials developing near the PSI emission.

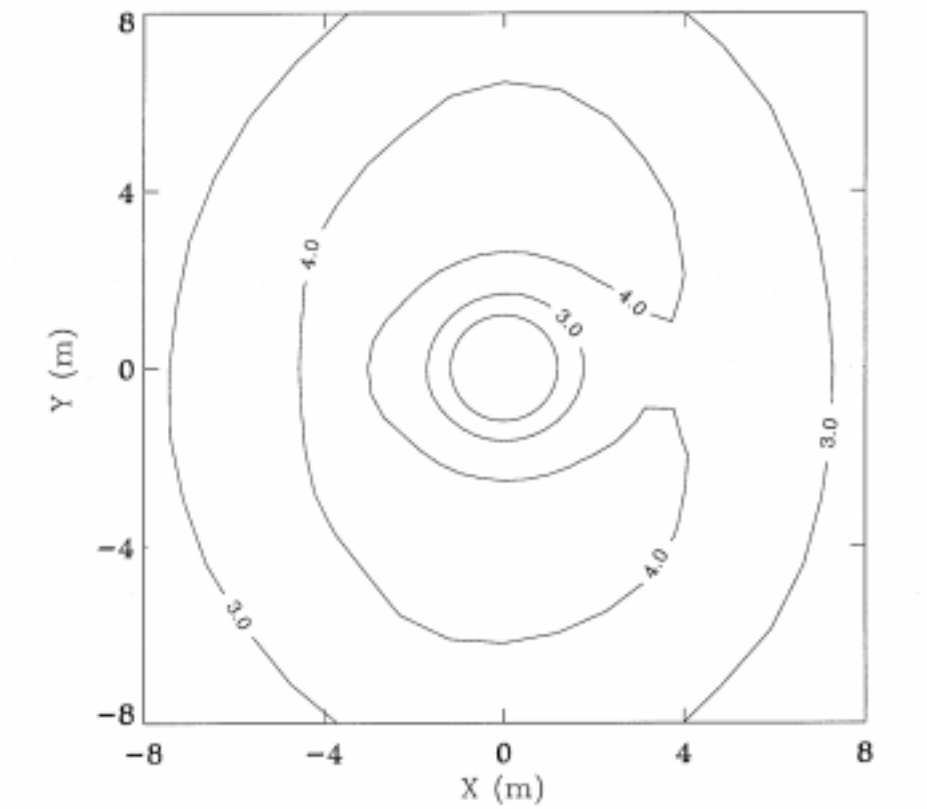


**Figure 7.** The potential contours in the x-y plane near the top (z=0.9m) surface of the satellite. Note that the potentials are relatively small near the top comparing to the bottom shown in Figure 6c.

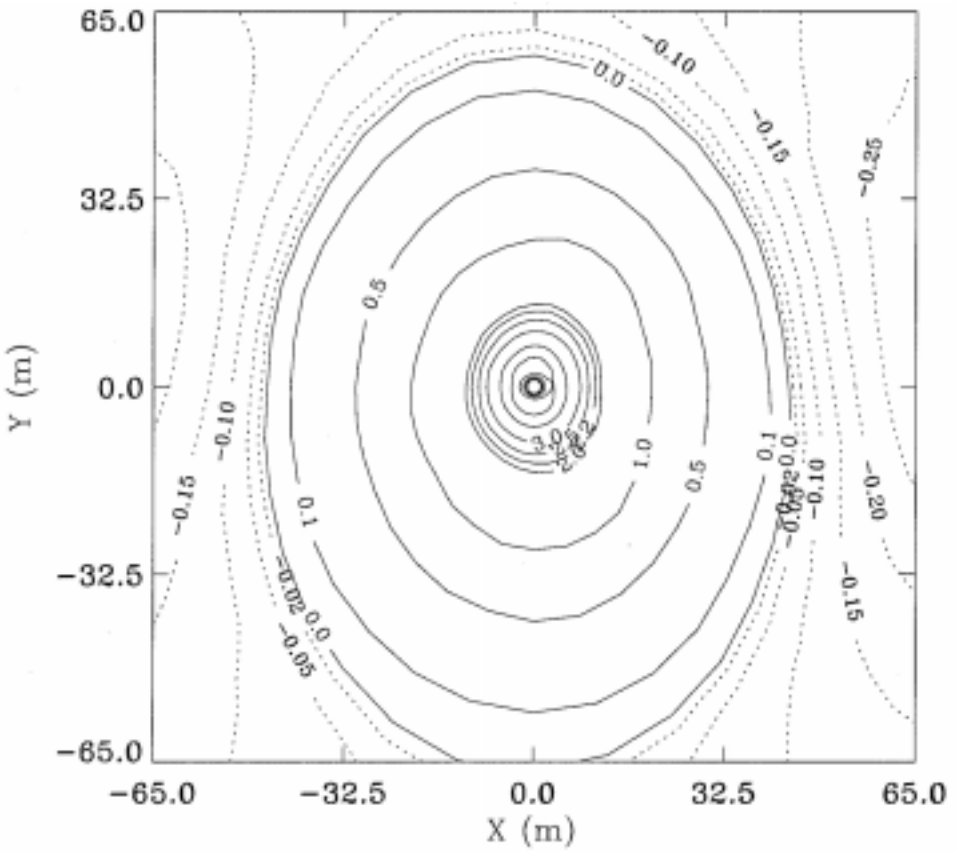


**Figure 8.** The potential contours in the x-y plane at z=0 up to a distance of 65m from the satellite. Note that an asymmetry is along y axis.

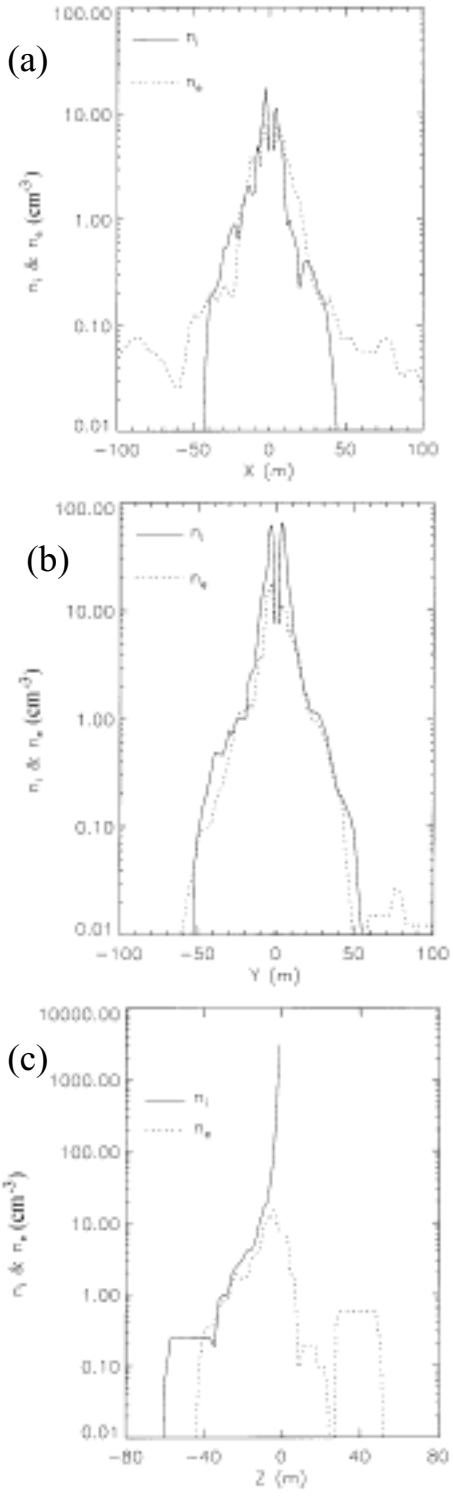


**Figure 9.** Plasma density distribution near the satellite along the three principal axes (a) x, (b) y, and (c) z, respectively. Note that the large densities develop below the PSI emission shown in (c).

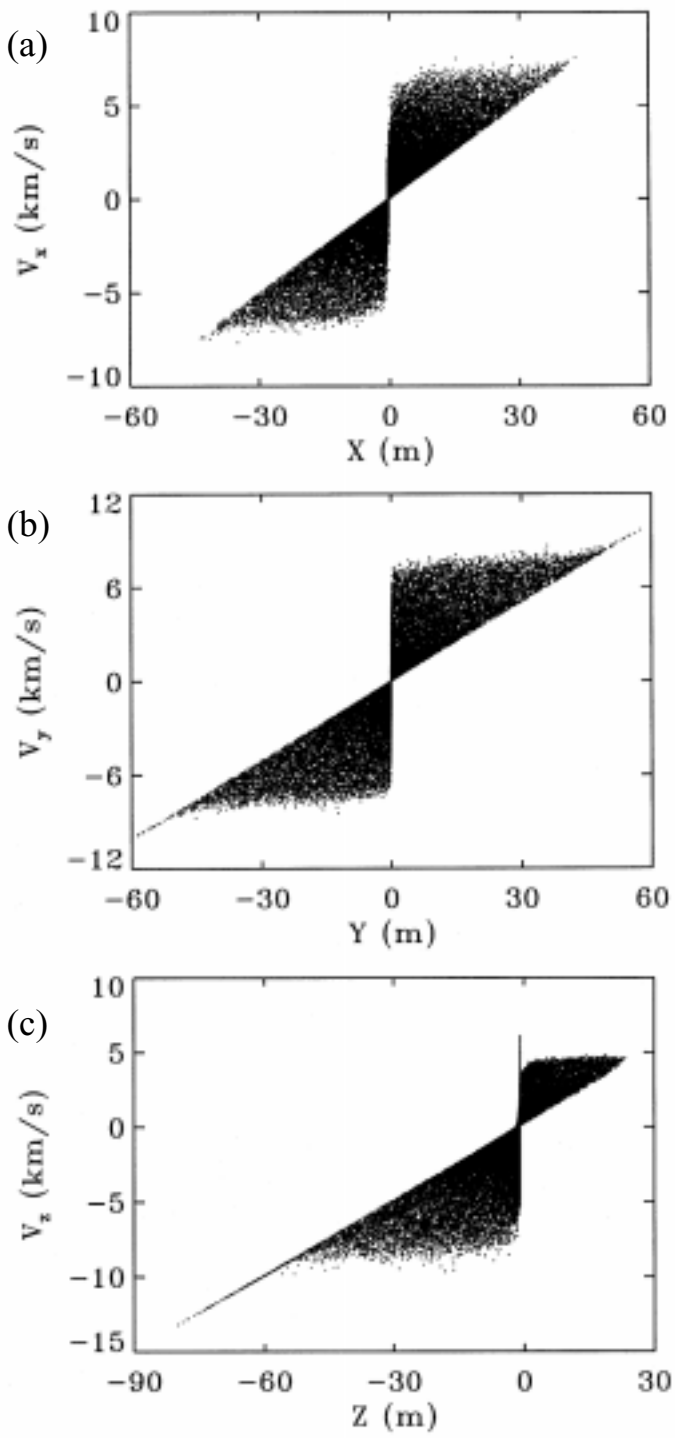


**Figure 10.** Ion phase space plots in (a) x-$V_x$, (b) y-$V_y$, and (c) z-$V_z$. Note the product of faster $Xe^+$ ions having velocity up to -13km/s.

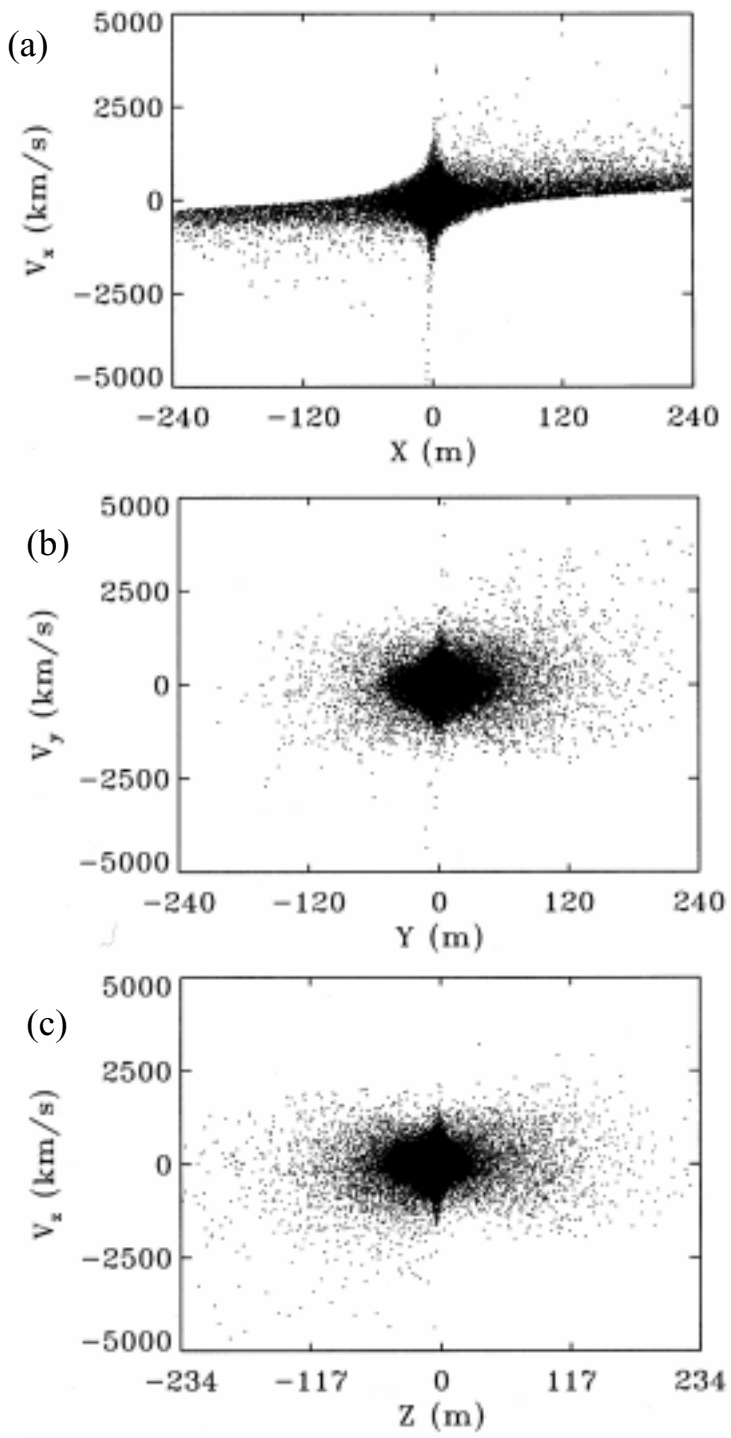


**Figure 11.** Electron phase space plots in (a) x-$V_x$, (b) y-$V_y$, and (c) z-$V_z$. Note the product of relatively fast electron having velocity up to 4000km/s.

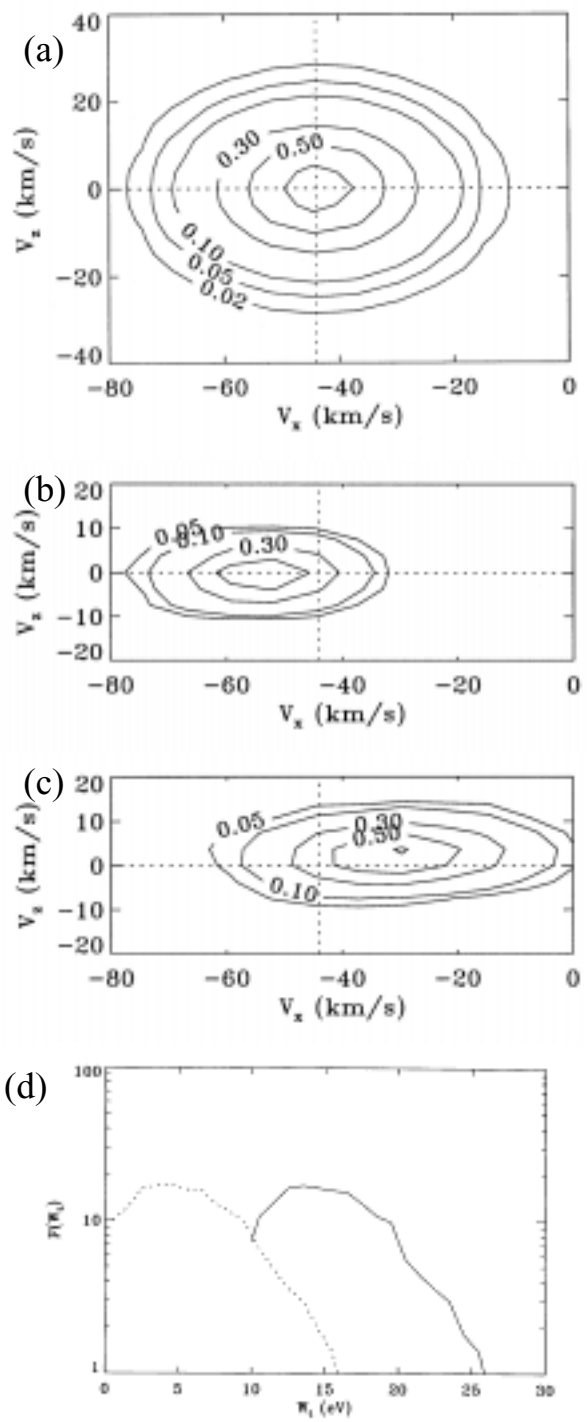


**Figure 12**. (a) The initial velocity distribution of the injected ions representing the ambient polar wind in $V_x$-$V_z$ plane. The beam energy is 10eV with an average beam velocity of -44.3km/s. (b) The initial, and (c) the final velocity distributions of ions which were eventually collected by the TIDE detector. Out of $1.2\times10^5$ $H^+$ ions injected in the boundary, only 170 ions were collected in the vicinity of TIDE. (d) The initial (solid line) and final (dotted line) kinetic energies of the collected ions. After collection ions lost 10eV energy.

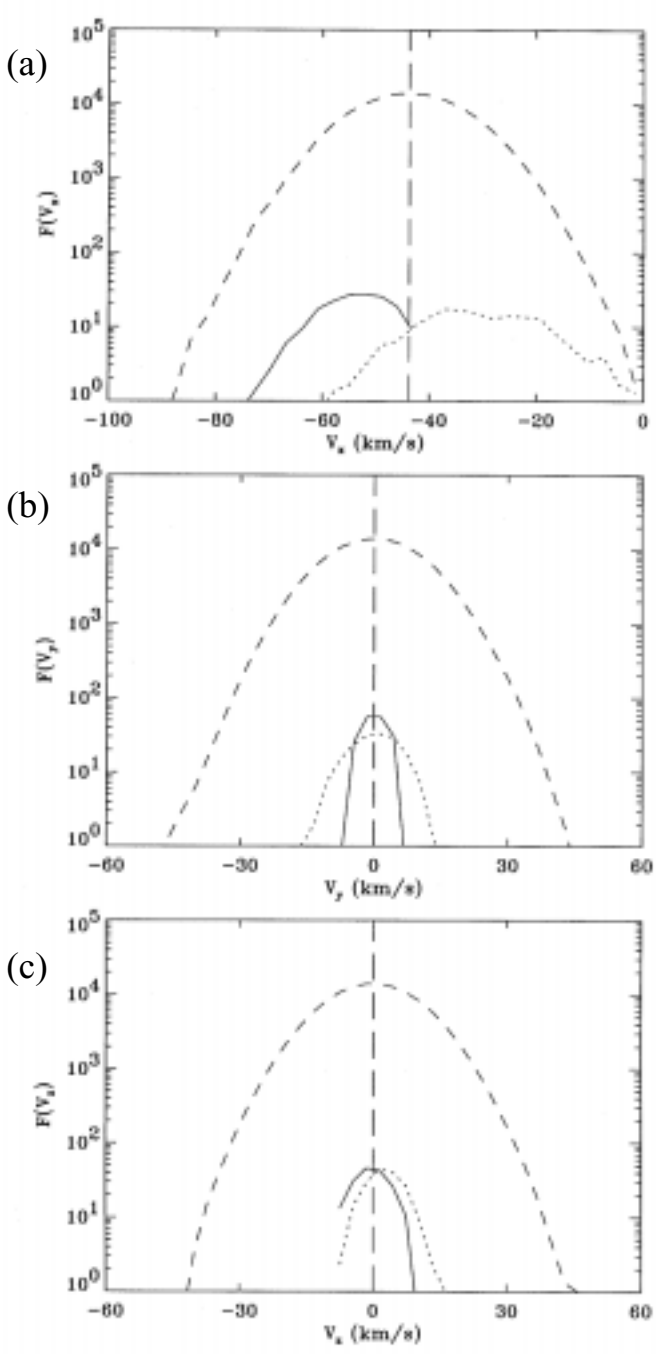


**Figure 13**. Ion distribution functions (a) $F(V_x)$, (b) $F(V_y)$, and (c) $F(V_z)$. Distributions of the initial injected ions are shown by dashed curves. The initial distribution of the ions eventually collected by TIDE by solid curves and after collection by dotted curves.

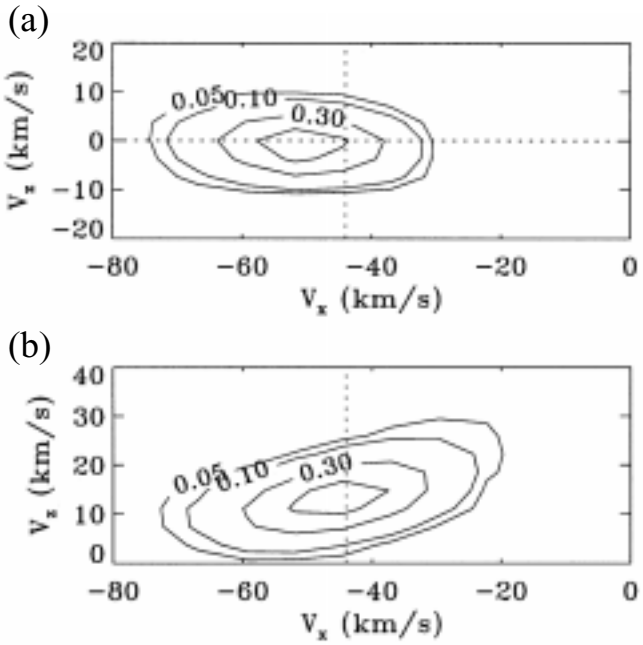


**Figure 14**. The velocity distribution of the collected ions in $V_x$-$V_z$ plane when PSI is on (a) initial in ambient polar wind and (b) final of the collection. The polar wind beam energy is 10eV.

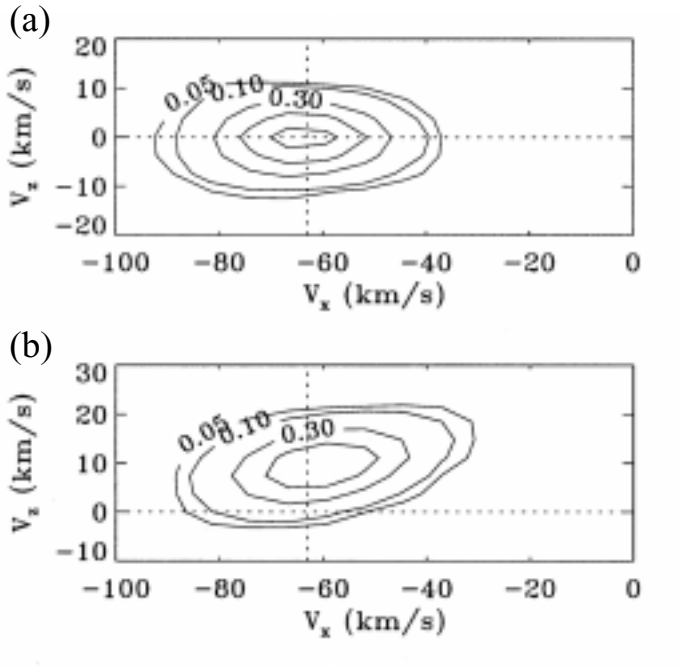


**Figure 15.** Same as Figure 14 but the polar wind beam energy is 20eV with an average beam velocity of –63km/s.

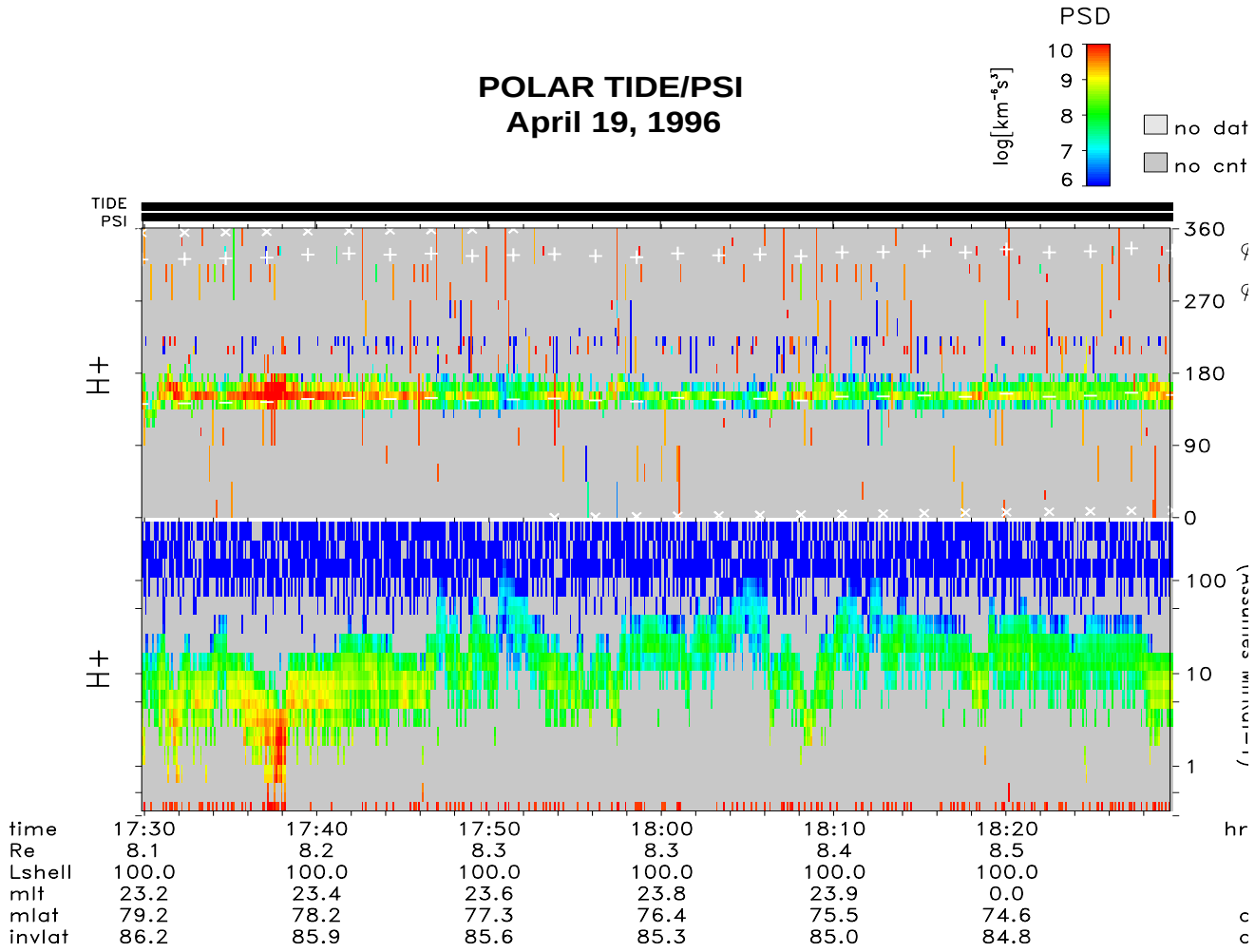


Figure 16. A spectrogram of H+ phase space density from the POLAR/TIDE instrument. The polar wind is seen as the narrow beam along the field line near 180 degrees in spin angle in the upper panel and at energies below about 100 eV in thelower panel.

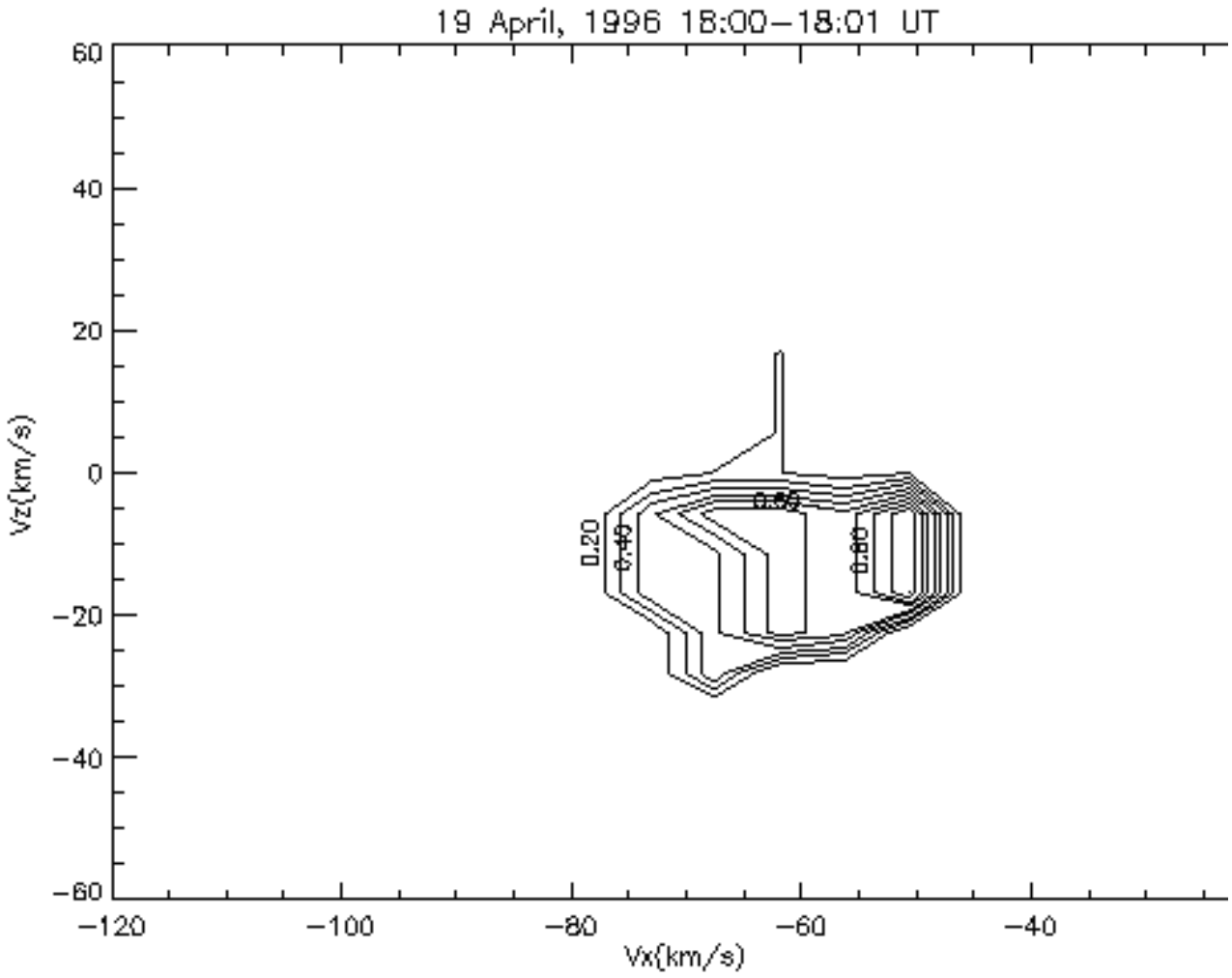


Figure 17. Contours of normalized H+ phase space density measured by TIDE. The contours were made from the measurements taken from 1800 UT to 1801 UT in Figure 16.

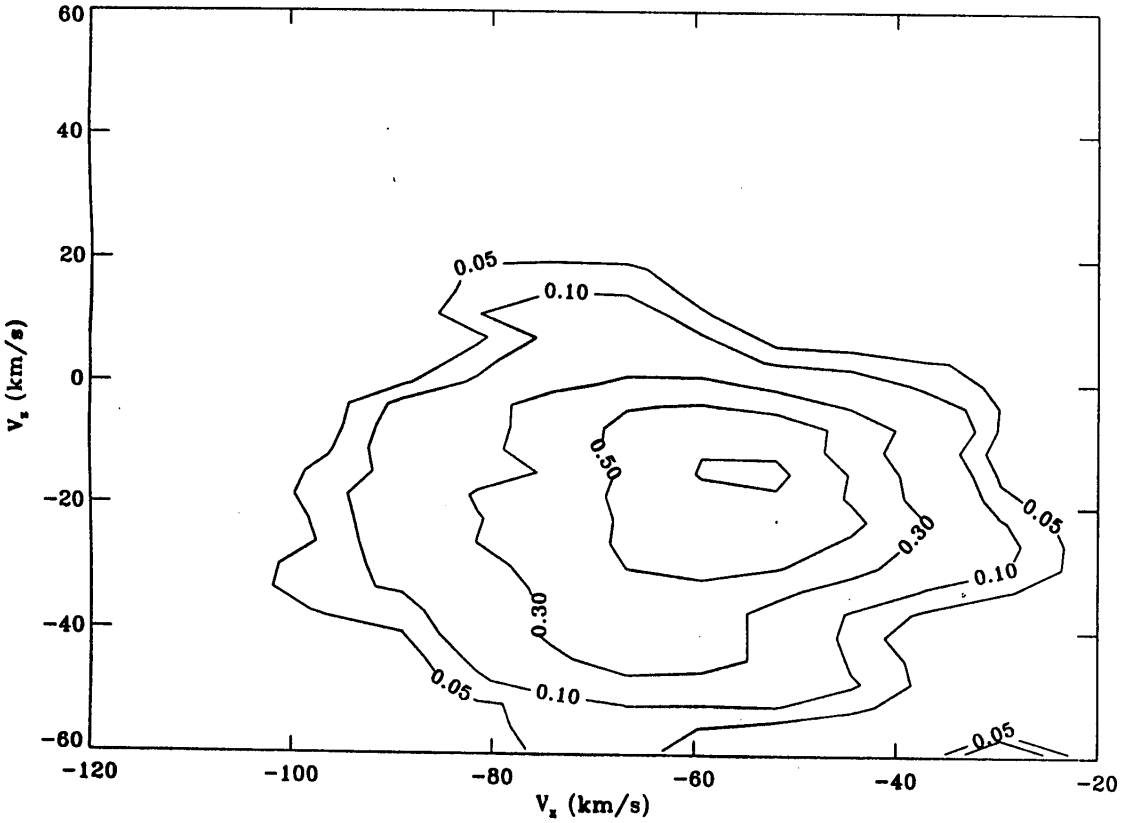


Figure 18. Normalized contours of the velocity distribution from the simulations. Parameters are the same as in Figure 15 but with a 20 km/s drift in the negative z direction.